



Repositorio Institucional de la Universidad Autónoma de Madrid

<https://repositorio.uam.es>

Esta es la **versión de autor** del artículo publicado en:
This is an **author produced version** of a paper published in:

ACS Nano 14.4 (2020): 4122-4133

DOI: <https://doi.org/10.1021/acsnano.9b08824>

Copyright: © 2020 American Chemical Society

El acceso a la versión del editor puede requerir la suscripción del recurso

Access to the published version may require subscription

In Vivo Spectral Distortions of Infrared Luminescent Nanothermometers Compromise Their Reliability

Yingli Sher^a, José Lifante^{b,c}, Nuria Fernández^{b,c}, Daniel Jaque^{a,c}, Erving Ximendes^{a,c}*

^a Fluorescence Imaging Group, Departamento de Física de Materiales – Facultad de

Ciencias, Universidad Autónoma de Madrid, C/Francisco Tomás y Valiente 7, Madrid

28049, Spain

^b Fluorescence Imaging Group, Departamento de Fisiología – Facultad de Medicina,

Avda. Arzobispo Morcillo 2, Universidad Autónoma de Madrid, Madrid 28029, Spain

^c Nanobiology Group, Instituto Ramón y Cajal de Investigación Sanitaria, IRYCIS, Ctra.

Colmenar km. 9.100, Madrid 28034, Spain

Corresponding author's e-mail: daniel.jaque@uam.es

ABSTRACT

Luminescence nanothermometry has emerged over the last decade as an exciting field of research due to its potential applications where conventional methods have demonstrated to be ineffective. Preclinical research has been one of the areas that have benefited the most from the innovations, proposed in the field. Nevertheless, certain questions concerning the reliability of the technique under *in vivo* conditions have been continuously overlooked by most of the scientific community. In this proof-of-concept, hyperspectral *in vivo* imaging is used to explain how unverified assumptions about the thermal dependence of the optical transmittance of biological tissues in the so-called biological windows can lead to erroneous measurements of temperature. Furthermore, the natural steps that should be taken in the future for a reliable *in vivo* luminescence nanothermometry are discussed together with a perspective view of the field after the findings here reported.

KEYWORDS: nanoparticles, nanothermometry, luminescent thermometry, tissue, attenuation, sensitivity

Minimally invasive high-resolution *in vivo* thermal sensing is highly desired by biomedical researchers working in preclinical studies. Among the different reasons that drew the attention of the scientific community to this specific application was the fact that contactless thermometry could be used as a tool for the early diagnosis of several diseases as well as for improving the efficacy of thermal therapies.^{1–5} As a consequence, there has been a fast development of what is now called luminescence nanothermometry (LNTh). LNTh is based on the use of luminescent nanoparticles (LNPs) whose spectroscopic properties are thermally dependent in the physiological range of temperature (10–50 °C).^{6–20} Different fluorescent compounds, including organic dyes, fluorescent proteins and a large variety of NPs (metallic, dielectric doped with rare-earth ions, quantum dots, *etc.*), have already been successfully used for *in vivo* remote thermal sensing.^{21–23} When compared to other thermometry methods, LNTh presents the advantage of being minimally invasive, cost-effective and experimentally simple.

Although LNTh is in its early stages, a good number of preclinical applications have already been demonstrated thanks to the appearance of luminescent nanothermometers

working in the spectral ranges known as biological windows (BW_s),^{24–34} where absorption and scattering of light in biological tissues are minimized.^{35–42} They have made possible: deep abdominal temperature sensing,⁴³ *in vivo* recording of subcutaneous thermal videos,^{44,45} and the identification of incipient diseases (such as ischemia or tumors).^{46–48} Thereupon, the scientific community became aware of the necessity to enhance the properties (such as brightness or thermal sensitivity) of the available luminescent thermometers. Nevertheless, certain questions concerning their reliability are now arising.⁴⁹ It has been reported, for instance, that some artefacts may arise from system inhomogeneities,⁵⁰ from the limitations of the detection system,⁵¹ from the interference of contaminants or external signals,⁵² and/or from an unexpected dependence of the system's response under the experimental conditions.^{53,54} The partial self-absorption (SA) of luminescence (*i.e.* when there is an overlap between the excitation and emission spectra) could also be a factor that alters the spectral shape of rare-earth-based LNTHs and, to some degree, of dyes and QDs.⁴⁹

While *in vivo* conditions generally impose many other factors (such as vascular blood flow, nanoparticle aggregation and biodistribution) that might affect the measurements performed with luminescent probes, there is an artefact that remains overlooked by the scientific community. In general, it is simply assumed that if one designs a luminescent nanothermometer that operates in the BWs, the interplay between the tissue-induced attenuation and the luminescence that carries the thermal information can, in a good approximation, be neglected. This assumption implies that the collected luminescence has the same spectral properties as the luminescence generated by the deep-tissue allocated nanothermometers. Though the low attenuation coefficient of tissues in the BWs assures a maximized penetration depth of light, it does not guarantee the lack of spectral distortions. In fact, under most *in vivo* experimental conditions, the wavelength dependence of the optical properties of a tissue could give rise to such distortions.^{55–59} They, in turn, could yield valuable information, for instance, on the oxygenation state and structure of a tissue.^{60,61}

LNTh depends on the experimental determination of spectroscopic parameters such as (i) luminescence intensity, (ii) luminescence intensity ratio (LIR), (iii) spectral bandwidth, and (iv) wavelength position of an emission line.⁶ Therefore, it is reasonable to think that the thermal readouts obtained with this technique could be affected by the tissue-induced spectral distortions. Yet, when retrieving the literature, to the best of our knowledge, it is not possible to find any work connecting those two concepts. This could be mostly attributed to the lack of spectral resolution in the majority of infrared imaging equipment utilized for *in vivo* imaging. Indeed, the detection of *in vivo* tissue-induced spectral distortions is not an easy task at all. Recently, however, Hyperspectral Imaging (HSI) has been presenting itself as an automated spectrally sensitive technology that integrates imaging and conventional spectroscopy in such a way that it provides complementary information from both domains.^{62–67} Furthermore, given its intrinsic spatial resolution capability, the time needed for the studies of propagation of light in materials is reduced. This technology, therefore, could, in principle, be easily applied to gather information on attenuation-induced spectral distortions.

In this work, *in vivo* HSI is used to experimentally evaluate the magnitude of the tissue-induced spectral distortions in the luminescence of acclaimed infrared nanothermometers. An explanation of such phenomena is given in terms of the optical properties of several tissues. The implications that these results have and the next steps that should be taken in the field of luminescent thermometry are also discussed in detail.

RESULTS AND DISCUSSION

Hyperspectral Imaging in a Small Animal Model

The HSI system used in this work for the acquisition of luminescence spectra generated by nanothermometers is schematically depicted in **Figure 1a**. Briefly speaking, optical excitation was provided by an 800 nm fiber-coupled laser diode. A short-pass filter was used to block the long-wavelength tail of the laser source. The scattered light emitted from the sample was transmitted through a long-pass filter (Thorlabs FL0850) that was intended to suppress the reflected laser signal. Shortwave Infrared (SWIR) lenses were then used as a relay to image the pupil on a Bragg Tunable Filter (BTF) which, in turn, would select a specific wavelength, λ , of the coming light.⁵⁵ This filtered light was then

focused, by a second lens, on an infrared camera (ZephIR™ 1.7) to produce a monochromatic image. Synchronous tuning of the BTF and image acquisition allowed the obtainment of monochromatic fluorescence images corresponding to different emission wavelengths ranging from 900 up to 1700 nm. Under those circumstances, a 3D spatial map of spectral variation, *i.e.* a HSI cube, was built: the first two dimensions provided spatial information and a third dimension accounted for the spectral information.^{56–58,68} The intensity values of a particular pixel in a HSI cube characterized its spectral fingerprint. As an example, the HSI cube of a colloidal solution of Ag₂S dots is shown in **Figure 1b**, from which their emission spectrum is obtained.

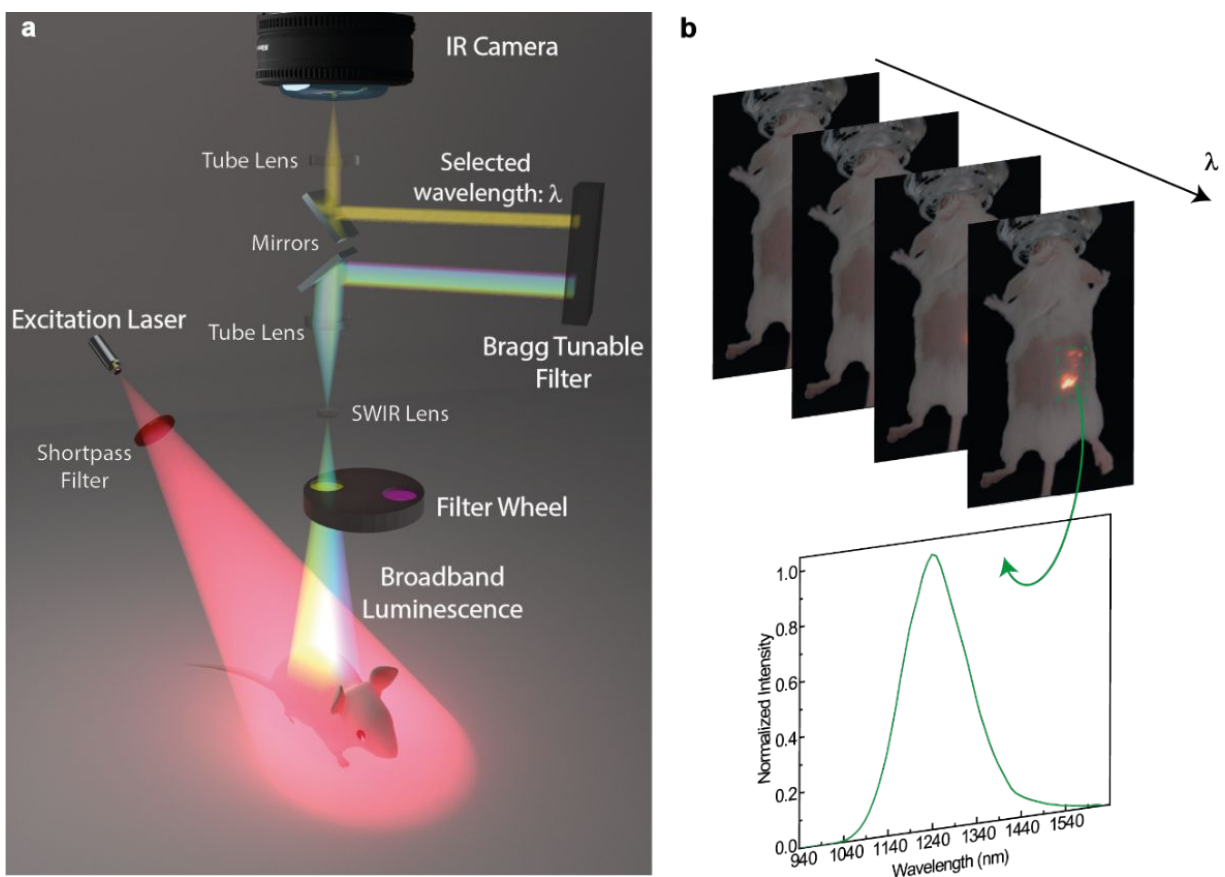


Figure 1. Hyperspectral Imaging. **a)** Schematic representation of the hyperspectral imaging system used in this work. **b)** Representative stack of narrowband sub-images of a mouse injected with Ag_2S dots superimposed to its optical photo. The images from a 3D hypercube from which one obtains the emission spectrum corresponding to a selected region.

Tissue-Induced Spectral Distortions

If an optically excited luminescent nanothermometer is under a tissue of thickness L then, according to the Modified Beer-Lambert Law, which is here introduced not as a complete description of the light-tissue interaction but rather as a didactic tool for the sake of the discussion, the luminescence intensity at wavelength λ detected ($I_{det}(\lambda)$) after passing through the tissue is given by:^{69–72}

$$I_{det}(\lambda) = I_o(\lambda)e^{-g(\lambda,L) - L \times [\sum_i \epsilon_i(\lambda) \times DPF(\lambda)]} \quad (1)$$

where $I_o(\lambda)$ is the actual luminescence intensity generated by the nanothermometers at wavelength λ , g is a function that depends on the geometry of the tissue and that accounts for the light intensity loss due to scattering, ϵ_i is the molar extinction coefficient of the i -th chromophore found in the tissue and DPF is the *Differential Pathlength Factor* (*i.e.* a parameter that accounts for increases in optical paths). Eq. 1 clearly states that $I_{det}(\lambda) \neq I_o(\lambda)$. In general, past works considered that the relationship between the detected and the emitted signals was determined by a single constant of proportionality (*i.e.* $I_{det}(\lambda) = k \cdot I_o(\lambda)$, with $0 < k < 1$). This implies that the extinction coefficient of a tissue is wavelength-independent, which is known to be false. In spite of this, the impact that tissue absorption

has on the shape of the detected luminescence generated by nanothermometers has remained unexplored. To work around this problem, a simple experiment with two CD1 mice was firstly designed. The first mouse was subjected to a subcutaneous injection of Ag_2S dots while the second one was subjected to an intravenous injection of a solution of Ag_2S dots. More details can be found in the Methods Section. **Figure 2a** and **2b** show the fluorescence images obtained in each case for an emission wavelength of 1200 nm. In the latter, the signal was generated by Ag_2S dots accumulated in the liver. The normalized luminescence spectra obtained from the HIS cubes obtained in each case are shown in **Figure 2d** and **2e**. The original spectra are included in **Section S1** of Supporting Information. While the subcutaneous injection provides a luminescence spectrum almost identical to the one generated by Ag_2S dots in colloidal solution (broad and symmetric band centered at around 1240 nm), the detected emission spectrum corresponding to the NPs accumulated in the liver differs by a great amount. In principle, this spectral distortion could be attributed to either the tissue absorption or to a modification of Ag_2S dots in the liver due to, for instance, pH change. To rule out this second possibility, the mouse subjected to intravenous injection was sacrificed. The *ex vivo* fluorescence image and

spectrum of the liver are shown in **Figure 2c** and **2f**, respectively. As one can notice, there is an obvious similarity with the original spectrum of Ag₂S dots. This concludes that Ag₂S dots have not been significantly modified when accumulated in the liver and that the *in vivo* spectral distortion obeys the wavelength-dependent attenuation of tissues between the liver and the detection system (including vessels, skin, *etc.*). Such a fact is further demonstrated with an extra experiment (described in **Section S2** of Supporting Information) in which the relative position of the animal was changed and the spectral shape of the detected luminescence of the Ag₂S NPs was observed to change with it. The data included in **Figure 2**, therefore, clearly state that tissue-induced spectral distortions cannot be neglected when interpreting NIR-II *in vivo* fluorescence images. Otherwise, the analysis could lead to erroneous conclusions.

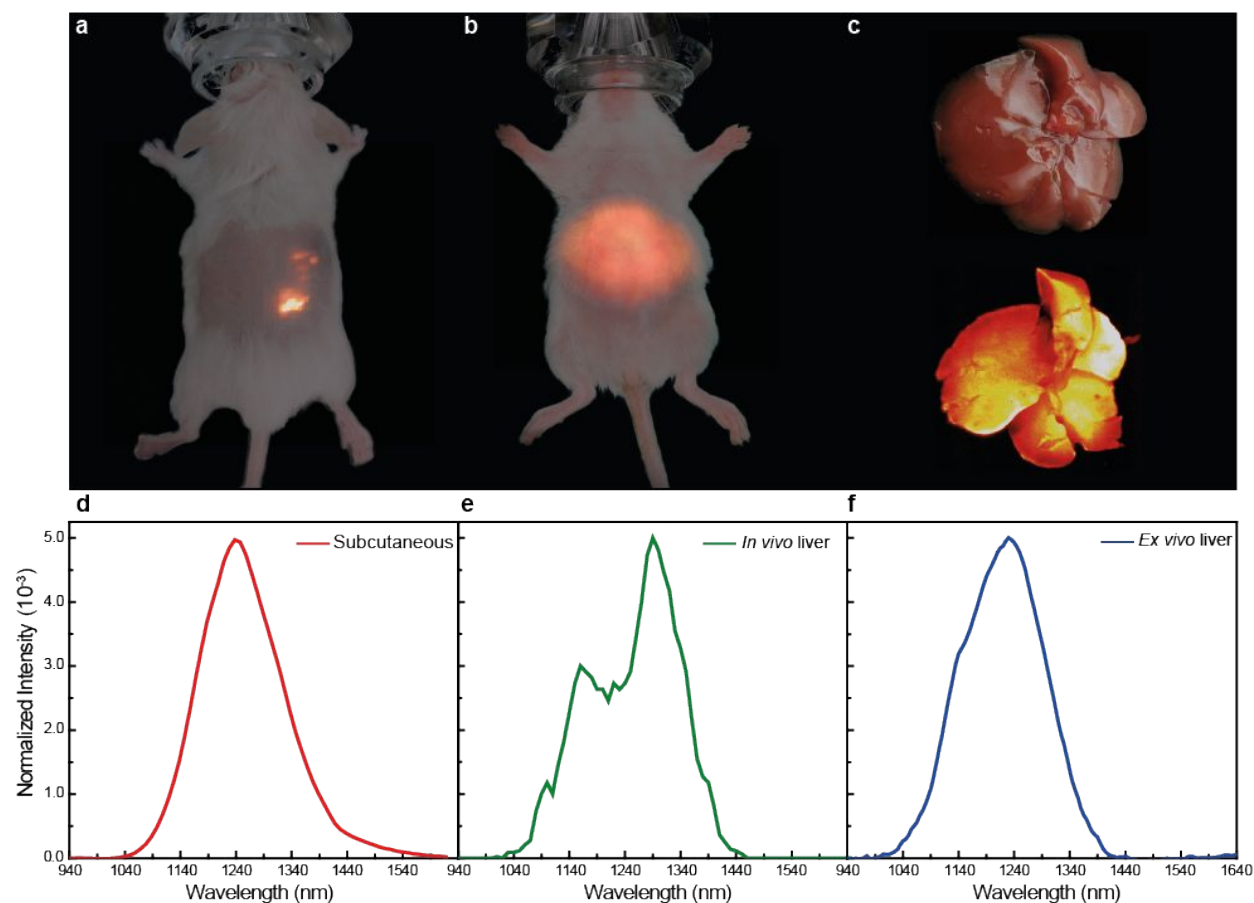


Figure 2. Spectral variations of Ag₂S dots under different conditions. Luminescence image generated by Ag₂S dots after **a)** a subcutaneous injection in a CD1 mouse, **b)** a retroorbital injection in a living mouse and **c)** sacrificing the mouse and isolating the liver (*ex vivo* conditions). Emission spectra of **d)** subcutaneous injection, **e)** retroorbital injection and **f)** isolated liver after retroorbital injection. The optical images of mouse and liver were included (or superimposed) in a, b and c for a better visualization. The spatial resolution of the measurement was $5.9 \times 10^{-2} \text{ mm}^2/\text{pixel}$.

Tissue-induced spectral distortions are not restricted to the case of Ag₂S dots. The performance of other infrared luminescent nanothermometers is also expected to be

affected. Though many probes have been proposed for *in vivo* thermal sensing, Yb@Nd LaF₃ and Er-Yb@Yb-Tm LaF₃ NPs were here selected as representative examples. They are, indeed, good systems to examine due to their good thermal sensitivity and broad ranges of emission inside the BWs.^{44,45,73} **Figures 3a** and **3b** show the broadband infrared luminescence images (850-1600 nm) of a cuvette filled with an aqueous solution of Yb@Nd LaF₃ NPs and of a mouse subjected to a subcutaneous injection of the same NPs, respectively. **Figure 3c** shows the normalized emission spectra obtained from the HSI cubes of the Yb@Nd LaF₃ NPs in a colloidal suspension and the Yb@Nd LaF₃ NPs subcutaneously allocated. The skin-induced distortions in the emission spectra are evident. Indeed, they affect the intensity ratio between emissions at 980 and 1060 nm which, in turn, is commonly used for thermal sensing. **Figure 3d** and **3e**, in turn, show the broadband infrared luminescence images (850-1600 nm) of a cuvette filled with an aqueous solution of Er-Yb@Yb-Tm LaF₃ NPs and of a mouse subjected to a subcutaneous injection of the same NPs, respectively. In this case, the skin-induced spectral distortions are even more evident than those observed for Ag₂S and Yb@Nd LaF₃ NPs (see **Figure 3f**). In particular, skin absorption leads to a relevant reduction in

the relative intensities of the emission bands centered at 1230 and 1470 nm, of Tm^{3+} , also used for ratiometric thermal sensing.

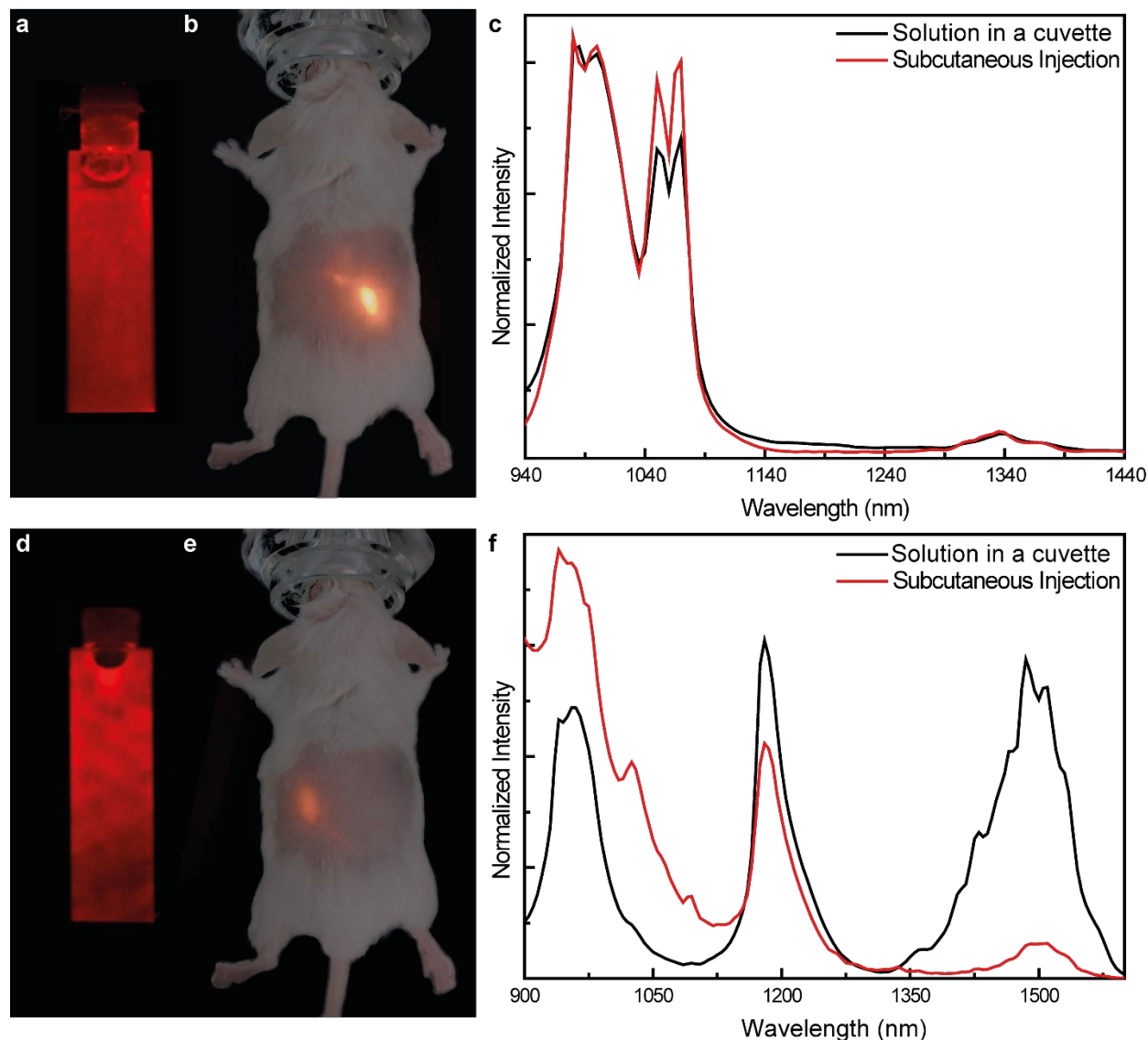


Figure 3. Luminescence of Yb@Nd LaF₃ NPs and SWCNTs subcutaneous injections. Luminescence images of **a)** cuvette containing Yb@Nd LaF₃ NPs, **b)** subcutaneous injection of Yb@Nd LaF₃ NPs in a living mouse, **c)** cuvette containing Er-Yb@Yb-Tm LaF₃

NPs and **d)** subcutaneous injection of Er-Yb@Yb-Tm LaF₃ NPs in a living mouse. Emission spectra of the cuvette and subcutaneous injection corresponding to **e)** Yb@Nd LaF₃ NPs and **f)** Er-Yb@Yb-Tm LaF₃ NPs. The optical image of the mouse was superimposed in **b** and **d** for a better visualization. The spatial resolution of the measurement was 5.9×10^{-2} mm²/pixel.

Figures 2 and 3 clearly reveal how the optical attenuation caused by skin could lead to relevant spectral distortions in subcutaneously injected luminescent nanothermometers.

However, when dealing with other applications (such as brain thermometry), different contributions to the net optical attenuation should be expected due to the presence of distinct tissues. Since discriminating the roles played by different biological tissues under *in vivo* conditions is a task that would involve the knowledge of several uncontrolled factors (such as nanoparticles aggregation and vascular blood flow), some *ex vivo* experiments were conducted to provide an approximation of the real problem. Thin pieces of different tissues (taken from a group of sacrificed CD1 mice) were put on the surface of a cuvette containing solutions of either Ag₂S dots, Yb@Nd LaF₃ NPs or Er-Yb@Yb-Tm LaF₃ NPs. HSI cubes were then measured and the luminescence spectra as obtained in presence of different tissues were recorded. **Section S3** of Supporting Information

contains some of the monochromatic HSI images taken throughout the experiment.

Figure 4a, b and c include, as representative examples for each type of NP, the emission spectra in the absence of any tissue, in the presence of a 2 mm thick skin sample and in the presence of a 2 mm thick cortex tissue. In all the cases, the presence of the tissues leads to a significant spectral distortion. In order to quantify it, the percentage difference, σ , in the spectral shape with respect to the non-affected spectrum was calculated. This parameter is defined as:

$$\sigma_{tissue} = \int |I_{tissue}^{norm}(\lambda) - I_{non-att}^{norm}(\lambda)| d\lambda \quad (2)$$

where the sup-index *norm* indicates that the spectrum was normalized to the area (*i.e.*

$I_{norm}(\lambda) = I(\lambda) / \int I(\lambda) d\lambda$), I_{tissue} and $I_{non-att}$ stand for the spectra obtained with and without

the tissue, respectively. The results are summarized in **Figure 4 d, e and f** where σ was

analyzed for skin, muscle, skull, cortex, cerebellum and brainstem for Ag₂S dots, Yb@Nd

LaF₃ NPs and Er-Yb@Yb-Tm LaF₃ NPs, respectively. As one can see, the variation on

the shape of the spectra is more pronounced in some tissues than in others and it

depends on the spectral regions that the luminescent nanothermometers emit. The

transmitted luminescence of Er-Yb@Yb-Tm LaF₃, for instance, is the one which is mostly

affected, due to the overlap of its emission with the water absorption peaks at 980 and 1500 nm. The minimal value measured for the percentage difference was found to be close to 4% (skull in **Figure 4f**). Such results are compared with numerical simulations, considering the values of absorbance and transmittance of general tissues as provided by literature, in **Section S5** of Supporting Information.

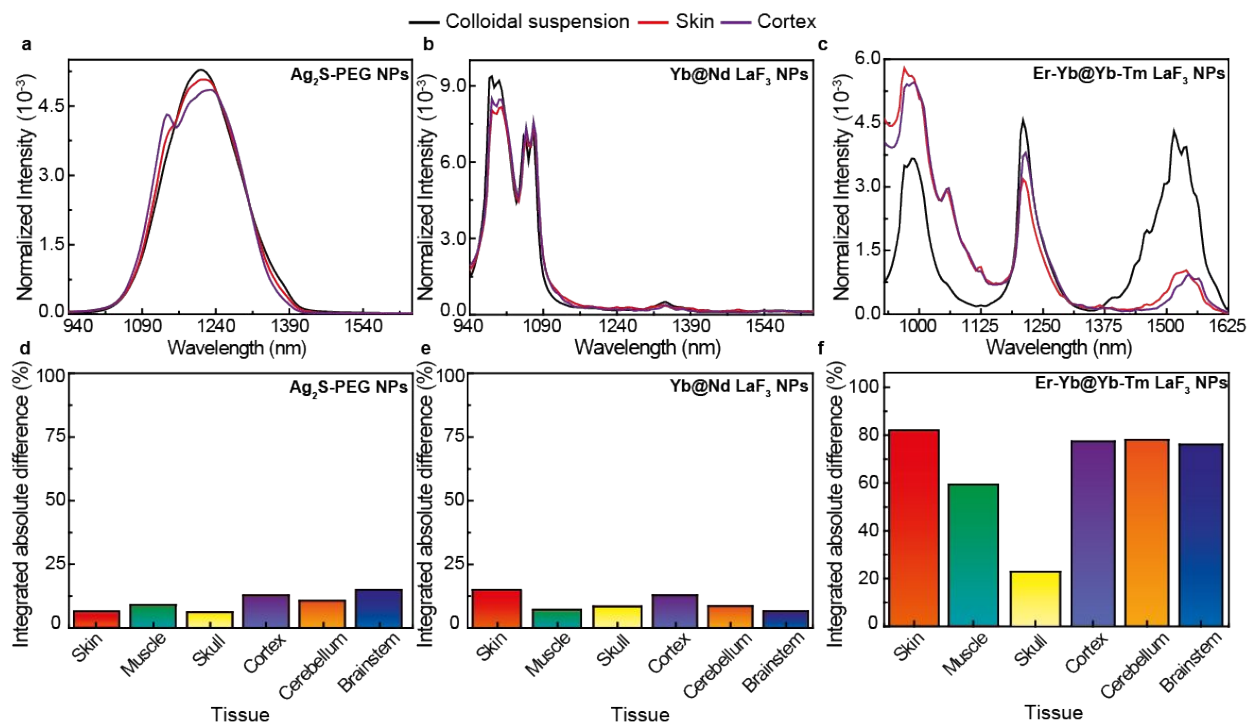


Figure 4. Tissue-induced changes in luminescence spectra of different NPs. Luminescence spectra of different cuvettes containing a solution of either **a)** Ag₂S NPs, **b)** Yb@Nd LaF₃ NPs or **c)** Er-Yb@Yb-Tm LaF₃ NPs when having no tissue (black), skin tissue (red) or brain cortex (purple) on their surfaces. Tissue-induced percentual difference of luminescence spectrum shape of **d)** Ag₂S NPs, **e)** Yb@Nd LaF₃ NPs and **f)** Er-Yb@Yb-Tm LaF₃ NPs. The spatial resolution of the measurement was 6.1×10^{-3} mm²/pixel.

Impact on Thermometry

Figure 4 raises a serious limitation of luminescent nanothermometers to provide absolute temperature readouts. Despite its apparent insignificance, even small percentage differences in the emission spectra caused by tissue-induced distortions could lead to relevant deviations in the absolute thermal readout. In fact, depending on the selected thermometric parameter Δ , the error in the temperature estimation, δT , could be of the same order of magnitude as σ/S , where S is the relative thermal sensitivity of the thermometer (defined as $\frac{1}{\Delta} \left| \frac{d\Delta}{dT} \right|$). Given that most of luminescent thermometers that operate in the BWs present a relative thermal sensitivity of the order of $1\% \text{ } ^\circ\text{C}^{-1}$, a σ of 4% could lead to an error of $\pm 4 \text{ } ^\circ\text{C}$ in the measurement of the absolute temperature. In worse scenarios, such as the case of Er-Yb@Yb-Tm LaF₃ NPs, this error could be magnified due to their higher values of σ .

A good number of recently proposed applications of luminescent nanothermometers mostly deals with measurements of temperature variations rather than absolute

temperature determination. This is the case of *in vivo* thermal transient studies or thermal control during tumor ablation.^{74,75} Nevertheless, several works have reported that the optical properties of tissues (specially its transmittance) could be temperature-dependent.^{76–84} Consequently, tissue-induced distortions in the emission spectra of luminescent nanothermometers would also be a function of temperature. This, in turn, could compromise the use of LNTh for *in vivo* determination of temperature variations. According to expression (1), if the molar extinction coefficient of the chromophores present in the tissue are temperature-dependent (*i.e.* $\epsilon_i = \epsilon_i(\lambda, T)$), then the *in vivo* calibration curve of any given nanothermometer would not only be given by the temperature variation of the thermometric parameter ($\frac{d\Delta}{dT}$) itself but also by the temperature variation of the tissue optical properties. In order to evaluate the importance of this second term, it is necessary to compare the calibration curves in the presence and absence of a biological tissue. Given that Ag₂S dots present the possibility of using the ratio, intensity or peak position as thermometric parameters with relatively high thermal sensitivities, this particular luminescent thermometer was selected for the following set of experiments. A

thin piece of tissue (2 mm) was placed on the surface of a micro-chamber containing a solution of Ag_2S dots. The brainstem was chosen as the representative tissue due to its high induced percentage difference in the spectral shape of Ag_2S dots (**Figure 4d**). The temperature of the microchamber (with and without tissue) was varied (**Figure 5a**) and the corresponding emission spectra were measured. Experimental details concerning the calibration are found in the Methods Section. Representative monochromatic luminescence images and emission spectra can be found in **Section S4** of Supporting Information. By choosing a specific thermometric parameter Δ and using the standardized definition of the relative thermal sensitivity ($S_\Delta = \frac{1}{\Delta} \left| \frac{d\Delta}{dT} \right|$), the analysis of the emission spectra in the presence/absence of tissue (as obtained at different temperatures) allowed us to determine the variation of S_Δ . Since each thermometric parameter can have a different dependence with T, for the sake of comparison their thermal derivatives were all obtained by considering polynomial interpolations of 3rd order. Clear differences are observed when using the emitted intensity at 1220 nm (*Int*, **Figure 5b**), the intensity ratio (*Ratio* = $\text{Int}_{1180\text{nm}}/\text{Int}_{1260\text{nm}}$, **Figure 5c**) or peak position (λ_{max} , **Figure 5d**) as thermometric

parameters. The data suggest a general decrease in S due to the presence of brainstem (a pattern that is followed by other tissues, as seen in **Figure S6** of Supporting Information). The greatest variation is found for S_{Int} , which provided an average decrease of $1.8\% \text{ } ^\circ\text{C}^{-1}$. S_{Ratio} and $S_{\lambda_{max}}$, on the other hand, presented average decreases of 0.2 and $0.03\% \text{ } ^\circ\text{C}^{-1}$, respectively.

As discussed in details in **Section S7** of Supporting Information, the experimentally observed variations in S_{Δ} can be mainly attributed to the temperature-dependent optical properties of tissues. Thus, Equation (1) can be re-written as:

$$I(\lambda, T, L) = I_o(\lambda, T) e^{-L \mu_{att}^{eff}(\lambda, T, L)} \quad (3)$$

where, for the sake of simplicity, $\mu_{att}^{eff}(\lambda, T, L) = [\sum_i \epsilon_i(\lambda, T) \times DPF(\lambda, T)] + g(\lambda, L, T)/L$ was defined as the effective attenuation coefficient. As one can check, both the attenuation and the absorption are now considered to depend with temperature. Under this form, it becomes easier to infer that the thermal dependence of μ_{att}^{eff} is the main reason for the observed changes in the value of S_{\square} . When selecting different thermometric parameters, $\mu_{att}^{eff}(\lambda, T)$ contributes to S_{\square} in a different way. According to **Section S8** of Supporting Information, if one denotes $S_{Int}^{att}(T)$ and $S_{Int}(T)$ as the thermal sensitivities relative to the

emitted intensity at temperature T in the presence and absence of tissues, respectively, one can write:

$$|S_{Int}^{att}(T) - S_{Int}(T)| \leq \left| L \frac{d\mu(\lambda_c, T, L)}{dT} \right| \quad (4)$$

At the same time, if one denotes $S_{Ratio}^t(T)$ and $S_{Ratio}(T)$ as the thermal sensitivities relative to the intensity ratio at temperature T in the presence and absence of tissues, one can write:

$$|S_{Ratio}^{att}(T) - S_{Ratio}(T)| \leq \left| L \frac{d[\mu(\lambda_1, T, L) - \mu(\lambda_2, T, L)]}{dT} \right| \quad (5)$$

Expression (4) states that the stronger the thermal dependence of μ_{att}^{eff} at a certain wavelength, the larger the difference between the relative thermal sensitivities obtained in the presence and absence of the tissue when using the absolute intensity as the thermometric parameter. On the other hand, expression (5) indicates that, when dealing with ratiometric thermal sensitivities, the critical parameter is the difference between the thermal derivatives of μ_{att}^{eff} as measured at the two wavelengths selected to compute the intensity ratio. This, in turn, might explain the reason for the smaller differences in S_{Ratio} when compared to S_{Int} obtained for Ag_2S dots (**Figure 5b** and **c**). In addition, it also shows the rational of developing reliable ratiometric LNTh by selecting two wavelengths with

similar thermal dependences of the effective attenuation coefficient, so that

$\frac{d[\mu(\lambda_1, T, L) - \mu(\lambda_2, T, L)]}{dT} = 0$. Therefore, the determination of spectral regions with equivalent $d\mu$

$(\lambda_c, T, L)/dT$ should be a matter of concern in future studies. At this point, it is worth

mentioning that the limits in $S_{\lambda_{max}}$ cannot be explicitly stated in inequalities due to the

strong dependence of λ_{max} on the original shape of the spectrum of the luminescent probe.

Nevertheless, if certain assumptions are made (see **Section S8** of Supporting

Information), similar inequalities may be obtained. Though the changes in the values of

the relative thermal sensitivities were observed after considering polynomial

interpolations of 3rd order, one can verify that they still exist even if one assumes a specific

fitting function for the thermometric parameters (**Section S6** of Supporting Information).

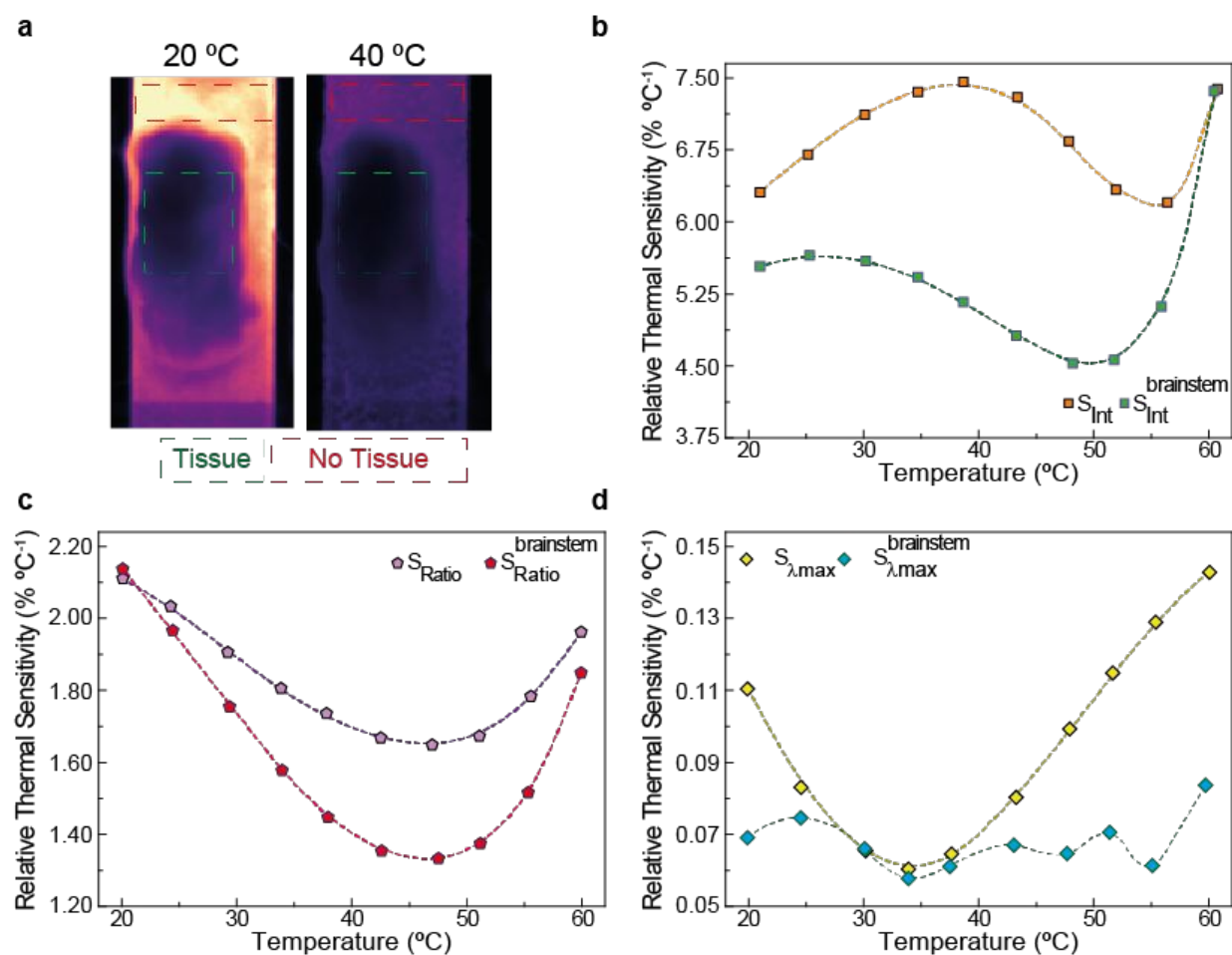


Figure 5. Tissue-induced changes in relative thermal sensitivity. **a)** Narrowband luminescence images (centered at 1200 nm) of a cuvette containing Ag₂S dots when having brainstem on its surface at 20 °C (top) and 40 °C (bottom). Comparison between the relative thermal sensitivity as measured in the presence and absence of tissue for **b)** absolute intensity, **c)** intensity ratio and **d)** peak position. Dashed lines were included as smoothed guide for the eyes. The spatial resolution of the measurement was 6.1×10^{-3} mm²/pixel.

Minimizing Erroneous Thermal Readouts

The impact on subtissue thermal sensing of the reported changes in the thermal sensitivity are here evaluated by a simple experiment. In it, a slice of brainstem (2 mm of thickness) was placed on the surface of a micro-chamber containing a solution of Ag₂S dots. The whole system (solution+tissue) was then subjected to a heating cycle (see Methods Section) and a dynamic comparison between the estimations of ΔT through the different calibrations curves (for *Int*, *Ratio* and λ^{max}) of **Figure 5** was performed. A thermographic camera was also utilized to record the surface temperature. The thermal transients included in **Figure 6a** were obtained by using the calibration curve of Ag₂S dots in the absence of any tissue, whereas **Figure 6b** does consider the calibration in the presence of brainstem. Several differences are perceived when comparing them. The first is that, independently of the thermometric parameter selected, $\Delta T(t)$ always seem to be underestimated when the tissue-induced effects are neglected (*i.e.* $\Delta T(t)$ seem higher in **Figure 6b**). The second difference to notice is that the thermal transients contained in **Figure 6b** are much closer to the one recorded by the thermographic camera. This, in turn, could indicate a better accuracy in the estimation as such a proximity is predicted by numerical models accounting for laser-induced heat in thin tissues (see **Section S10** of

Supporting Information). The better reliability of data in **Figure 6b** is further supported by the precision of the estimation of $\Delta T(t)$ *via* different thermometric parameters (*Int*, *Ratio* and λ^{max}). While in **Figure 6a** the three methods present discrepancies in ΔT as large as 11 °C, the data in **Figure 6b** reduces it to 6 °C.

The use of calibration curves obtained in the presence of a tissue, therefore, benefits luminescence thermometry in accuracy as well as precision. To make this asset clear, the average temperatures were estimated with the correct, $\langle T \rangle^{correct} = (T_{Int}^{correct} + T_{Ratio}^{correct} + T_{\lambda}^{correct})/3$, and incorrect calibrations, $\langle T \rangle^{incorrect} = (T_{Int}^{incorrect} + T_{Ratio}^{incorrect} + T_{\lambda}^{incorrect})/3$, in **Figure 6c**. Their respective standard deviations were plotted as error bars. As one can observe, when considering the tissue-induced effects, not only is the standard deviation smaller (*i.e.* improved precision) but, especially at longer time points, the distance to the values recorded by the thermographic camera is reduced (*i.e.* improved accuracy). Though these averages were calculated considering equal weights of reliability for each thermometric parameter, future studies on their relationship with the intrinsic experimental errors may point to a different direction.

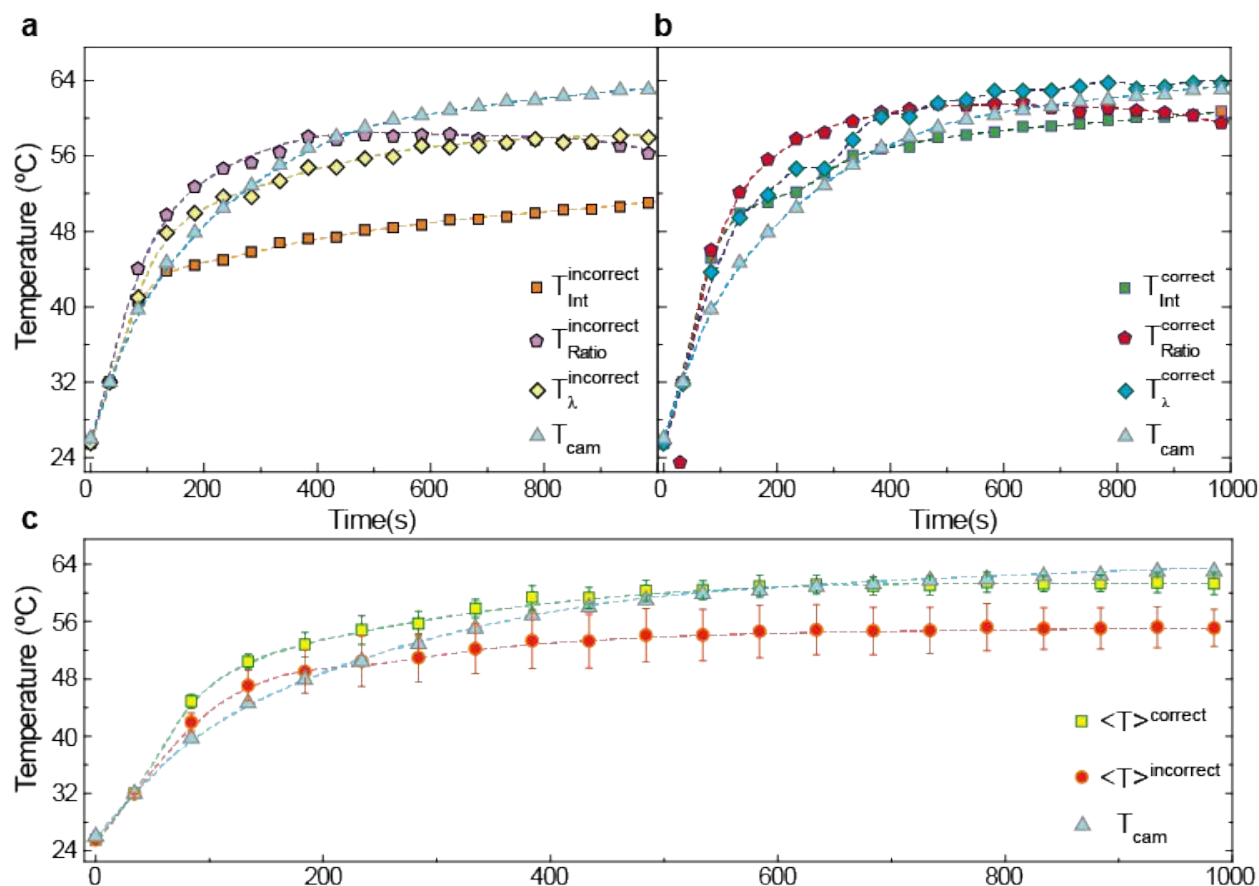


Figure 6. Tissue-induced changes in relative thermal sensitivity. Estimation of ΔT by different thermometric parameters when considering the calibration **a)** in the absence and **b)** presence of a tissue. **c)** Average temperature of the tissue as estimated according to the different calibrations (correct when considering the tissue, incorrect otherwise). Dashed lines were included as smoothed guide for the eyes. The temporal and spatial resolution of the measurement were 30s and $6.1 \times 10^{-3} \text{ mm}^2/\text{pixel}$, respectively.

Given the importance of the tissue-induced phenomena that were here presented, the question of how to reliably measure the temperature without the need of exhaustive acquisition of additional calibration curves persists as a complex puzzle (see Figure S12 of Supporting Information). The most investigative approach to the problem would consider the complete characterization of the thermal dependence of the optical properties of main tissues in the BWs. Under such circumstances one would only need to know the dimensions of the tissues in order to estimate the real temperature. A fully

pragmatic approach, on the other hand, would move the focus of the field to lifetime-based thermometry. Each of these positions have their own strengths and weaknesses. The former seems a universal but burdensome solution. The latter seems to be easier but applicable to only a certain type of luminescent thermometers. Ideally, more elaborate plans of solution should locate themselves in the middle ground of the two extremes. The decision over which plan must prevail will depend not only on its feasibility but also on the priorities set to the field of luminescence thermometry. Such discussion, however, is out of the scope of this work.

CONCLUSIONS

Hyperspectral *in vivo* imaging is here employed to investigate the role played by the tissue optical properties in *in vivo* luminescence thermometry. This work demonstrates that biological tissues, under various conditions, significantly distort the shape of the spectra of infrared luminescent probes operating within the biological windows. These distortions, in turn, could lead to erroneous thermal readouts. Results here reported also demonstrate how the presence of tissues lead to relevant changes in the calibration curves of luminescent nanothermometers and to thermal sensitivities significantly different from those obtained from aqueous solutions (traditionally used to estimate subtissue temperatures). All these effects are explained by considering the thermal dependence of light absorption and scattering processes in tissues. Simple experiments

reveal that the contribution given by the effective attenuation coefficient to the relative thermal sensitivity of luminescent nanothermometers strongly depend on the selected thermometric parameter. Though absolute emission intensity seemed to be the most affected one, the study of a heating transient in a tissue indicated that the changes in other parameters should not be so easily dismissed. In particular, we demonstrate how ratiometric thermal sensing, considered as the most reliable approach for remote thermal sensing, is also significantly affected by tissue-induced optical distortions.

This work demonstrates that *in vivo* luminescence nanothermometry is not as reliable as previously thought. It not only constitutes, as a proof of concept, a critical study on the field but it also proposes different ways of avoiding the negative impact that tissue-induced optical distortions have on the accurate determination of subtissue temperature.

Though much has been said about the need to consider the intrinsic error of measurements performed by luminescent thermometers (especially by means of quantities such as spatial and thermal resolutions),⁶ the direct assessment and explanation of the influence of tissue properties on the crucial parameter that is the relative thermal sensitivity had yet to be addressed. Based on the results here included,

future works dealing with *in vivo* luminescence thermometry should include different quality checks to ensure that the presence of the tissue is not leading to erroneous thermal readouts.

The impact of results here reported are not only restricted to *in vivo* luminescence thermometry. The magnitude of the here demonstrated *in vivo* tissue-induced spectral distortions should be also considered in other preclinical applications in which fundamental information is extracted from the spectral analysis of infrared emitting nanoprobe such as those works dealing with *in vivo* diagnosis through the spectral analysis of carbon nanotubes.⁵⁹

METHODS

Calibration measurements

When measuring the temperature calibrations, the system under study was put above a thermoelectrically Peltier plate cooled by a refrigerated circulating water bath (MX07R-20-A1 Heidolph) while being imaged by the equipment in Figure 1. Its temperature was then varied in the 20 °C -60 °C range, with a step of 5 °C, and 10 different HSI cubes were

obtained. A delay of 5 minutes between each measurement had to be considered for the achievement of thermal equilibrium.

Animal experiments

The *in vivo* experiments carried out in this work were approved by the Ethics Committee from Universidad Autónoma de Madrid (CEI) and complied with the principles of good laboratory animal care following the European Directive for the Protection of Animals Used for Scientific Purposes. For this study, two CD1 female mice (weight, 27 g; age, 8 weeks) were used. For the subcutaneous injection, 100 μL of an aqueous dispersion of NPs was used. A 25 gauge sterile needle was inserted to a depth of 1 cm under the pocket made by gently pulling up the skin over the flank. The injection depth was estimated to be 2 mm. The concentrations were 0.15 mg mL^{-1} for Ag_2S dots and 1.5 mg mL^{-1} for Yb@Nd LaF_3 NPs or Er-Yb@Yb-Tm LaF_3 NPs. Intravenous injection of Ag_2S dots (0.15 mg mL^{-1}) was performed through retro-orbital injection with a 27-G insulin needle and 1 mL syringe to deliver the NPs in the anesthetized mouse. Isoflurane was used as inhalant anesthetic (4% induction, 1% maintenance under a O_2 flow of 0.5 mL/min), and all the *in vivo* images were obtained with the animal under anesthesia. After

the experiments, euthanasia was performed by beheading with the animal under deep anesthesia (4% Isoflurane, O₂ flow of 0.5 mL/min for 2 minutes prior to beheading). For the Ag₂S experiments, the animals were sacrificed after 25 minutes of Ag₂S injection. The selection of 25 min as the ideal time to check the spectrum of the nanothermometers was motivated by preliminary experiments dealing with the biodistribution dynamics of intravenous injected Ag₂S nanoparticles in CD1 mice (**Section S13**).

Hyperspectral measurements

Right after sacrifice, fresh organs were immediately dissected and rinsed once with 0.9% NaCl isotonic saline solution to wash excessive blood. We then performed HyperSpectral imaging for the different organs under the following conditions: 5 second of exposure time, 5 nm of spectral resolution and maintained the laser power density as 50 mW/cm². Regarding the optical set up, one short-pass 850 nm filter (ThorLabs, FS850) was placed in front of the laser in order to filter the excitation wavelength around 808 nm. To minimize tissue-induced autofluorescence, two long-pass filters were placed, one 850 nm inside the lens (ThorLabs, FL850), and one 1100 nm in the diaphragm (ThorLabs, FL1100).

The response curves of the components of our detection system are included in **Section S12**.

Transient thermometry

The measurement of the *ex vivo* thermal transient was performed under the following conditions: the whole system (brainstem+micro-chamber) was put in the imaging system of **Figure 1** and excited by an 808 nm laser with high intensity (220 mW/cm^2) in such a way that its temperature would follow a heating transient. The subtissue temperature was estimated by the luminescence spectra of the luminescent nanoparticles. In the particular case of the data analyzed with the incorrect calibration, the initial temperature of the tissue was considered to be equal to the one initially measured by a thermographic camera (FLIR E40bx) that was coupled to the experimental setup, *i.e.* $\approx 25 \text{ }^\circ\text{C}$. The relative thermal sensitivity of the detected signal was then assumed to be independent of the presence of the tissue (see **Section S9** of Supporting Information).

ASSOCIATED CONTENT

Supporting Information:

The Supporting Information is available free of charge on the ACS Publications website at DOI: XXXX. It contains the information on (i) the unnormalized spectra obtained with a CD1 mouse and its liver after intravenous injection of NPs, (ii) the dependence of the spectral shape with the relative position of the animal, (iii) tissue-induced distortions in luminescence spectra, (iv) calibration with other brain tissues, (v) simulations on attenuation induced by tissues, (vi) estimation of relative thermal sensitivities with different fitting functions, (vii) calibration at different power densities, (viii) the mathematics behind the changes in thermal sensitivity due to tissue-induced effects, (ix) possible corrections in the analysis of temperature variations, (x) temperature distribution in thin tissues, (xi) response curves of the detection system and (xii) the optimal time to check the luminescence spectra of an intravenously injected NP.

AUTHOR INFORMATION

Author Contributions

The manuscript was written through contributions of all authors. All authors have given approval to the final version of the manuscript.

ACKNOWLEDGMENT

This work was supported by the Spanish Ministry of Economy and Competitiveness under projects MAT2016-75362-C3-1-R, MAT2017-83111R, and MAT2017-85617-R, by the Instituto de Salud Carlos III (PI16/00812), by the Comunidad Autónoma de Madrid (B2017/BMD-3867RENIMCM), and co-financed by the European Structural and investment fund. Additional funding was provided by the European Union's Horizon 2020 FET Open programme (grant agreement No 801305), the Fundación para la Investigación Biomédica del Hospital Universitario Ramón y Cajal project IMP18_38 (2018/0265) and also by COST action CA17140. Y. Shen acknowledges a scholarship from the China Scholarship Council (No. 201806870023).

REFERENCES

(1) Diederich, C. J. Thermal Ablation and High-Temperature Thermal Therapy: Overview of Technology and Clinical Implementation. *Int. J. Hyperthermia*. **2005**, *21*, 745–753.

- (2) Toutouzas, K.; Drakopoulou, M.; Dilaveris, P.; Vaina, S.; Gatzoulis, K.; Karabelas, J.; Riga, M.; Stefanadi, E.; Synetos, A.; Vlasis, K.; Stefanadis, C. Inflammation in Lone Atrial Fibrillation: New Insights by Coronary Sinus Thermography. *Int. J. Cardiol.* **2009**, *134*, 345–350.
- (3) Collins, A. J.; Ring, E. F.; Cosh, J. A.; Bacon, P. A. Quantitation of Thermography in Arthritis Using Multi-Isothermal Analysis. I. The Thermographic Index. *Ann. Rheum. Dis.* **1974**, *33*, 113–115.
- (4) Ng, E. Y.-K. A Review of Thermography as Promising Non-Invasive Detection Modality for Breast Tumor. *Int. J. Therm. Sci.* **2009**, *48*, 849–859.
- (5) Marin, R.; Skripka, A.; Besteiro, L. V.; Benayas, A.; Wang, Z. M.; Govorov, A. O.; Canton, P.; Vetrone, F. Heat Conversion: Highly Efficient Copper Sulfide-Based Near-Infrared Photothermal Agents: Exploring the Limits of Macroscopic Heat Conversion. *Small* **2018**, *14*, 1870238.

(6) Brites, C. D. S.; Lima, P. P.; Silva, N. J. O.; Millán, A.; Amaral, V. S.; Palacio, F.;

Carlos, L. D. Thermometry at the Nanoscale. *Nanoscale* **2012**, *4*, 4799–4829.

(7) Wang, X. D.; Wolfbeis, O. S.; Meier, R. J. Luminescent Probes and Sensors for

Temperature. *Chem. Soc. Rev.* **2013**, *42*, 7834–7869.

(8) Brites, C. D. S.; Balabhadra, S.; Carlos, L. D. Lanthanide-Based Thermometers: At

the Cutting-Edge of Luminescence Thermometry. *Adv. Opt. Mater.* **2019**, *7*, 1801239.

(9) Tzeng, Y.-K.; Tsai, P.-C.; Liu, H.-Y.; Chen, O. Y.; Hsu, H.; Yee, F.-G.; Chang, M.-S.;

Chang, H.-C. Time-Resolved Luminescence Nanothermometry with Nitrogen-Vacancy

Centers in Nanodiamonds. *Nano Lett.* **2015**, *15*, 3945–3952.

(10) Bastos, A. R. N.; Brites, C. D. S.; Rojas-Gutierrez, P. A.; DeWolf, C.; Ferreira, R.

A. S.; Capobianco, J. A.; Carlos, L. D. Thermal Properties of Lipid Bilayers Determined

Using Upconversion Nanothermometry. *Adv. Funct. Mater.* **2019**, 1905474.

(11) Kundu, S.; Mukherjee, D.; Maiti, T. K.; Sarkar, N. Highly Luminescent

Thermoresponsive Green Emitting Gold Nanoclusters for Intracellular Nanothermometry

and Cellular Imaging: A Dual Function Optical Probe. *ACS Appl. Bio Mater.* **2019**, *2*, 2078–2091.

(12) Liu, J. B.; Zhang, H.; Selopal, G. S.; Sun, S. H.; Zhao, H. G.; Rosei, F. Visible and Near-Infrared, Multiparametric, Ultrasensitive Nanothermometer Based on Dual-Emission Colloidal Quantum Dots. *ACS Photonics* **2019**, *6*, 2479–2486.

(13) Marin, R.; Vivian, A.; Skripka, A.; Migliori, A.; Morandi, V.; Enrichi, F.; Vetrone, F.; Ceroni, P.; Aprile, C.; Canton, P. Mercaptosilane-Passivated CuInS₂ Quantum Dots for Luminescence Thermometry and Luminescent Labels. *ACS Appl. Nano Mater.* **2019**, *2*, 2426–2436.

(14) Marciniak, L.; Bednarkiewicz, A.; Trejgis, K.; Maciejewska, K.; Elzbieciak, K.; Ledwa, K. Enhancing the Sensitivity of a Nd³⁺, Yb³⁺: YVO₄ Nanocrystalline Luminescent Thermometer by Host Sensitization. *Phys. Chem. Chem. Phys.* **2019**, *21*, 10532–10539.

(15) Wu, S. Y.; Min, H.; Shi, W.; Cheng, P. Multicenter Metal-Organic Framework-Based Ratiometric Fluorescent Sensors. *Adv. Mater.* **2019**, *32*, 1805871.

- (16) Ji, Z. L.; Cheng, Y.; Cui, X. S.; Lin, H.; Xu, J.; Wang, Y. S. Heating-induced Abnormal Increase in Yb³⁺ Excited State Lifetime and Its Potential Application in Lifetime Luminescence Nanothermometry. *Inorg. Chem. Front.* **2019**, *6*, 110–116.
- (17) Gschwend, P. M.; Starsich, F. H. L.; Keitel, R. C.; Pratsinis, S. E. Nd³⁺-Doped BiVO₄ Luminescent Nanothermometers of High Sensitivity. *Chem. Commun.* **2019**, *55*, 7147–7150.
- (18) Skripka, A.; Morinvil, A.; Matulionyte, M.; Cheng, T.; Vetrone, F. Advancing Neodymium Single-Band Nanothermometry. *Nanoscale* **2019**, *11*, 11322–11330.
- (19) Geitenbeek, R. G.; Nieuwelink, A.-E.; Jacobs, T. S.; Salzmann, B. B. V.; Goetze, J.; Meijerink, A.; Weckhuysen, B. M. *In Situ* Luminescence Thermometry to Locally Measure Temperature Gradients during Catalytic Reactions. *ACS Catal.* **2018**, *8*, 2397–2401.
- (20) Wylezich, T.; Sontakke, A. D.; Castaing, V.; Suta, M.; Viana, B.; Meijerink, A.; Kunkel, N. One Ion, Many Facets: Efficient, Structurally and Thermally Sensitive

Luminescence of Eu^{2+} in Binary and Ternary Strontium Borohydride Chlorides. *Chem. Mater.* **2019**, *31*, 8957–8968.

(21) Albers, A. E.; Chan, E. M.; McBride, P. M.; Ajo-Franklin, C. M.; Cohen, B. E.; Helms, B. A. Dual-Emitting Quantum Dot/Quantum Rod-Based Nanothermometers with Enhanced Response and Sensitivity in Live Cells. *J. Am. Chem. Soc.* **2012**, *134*, 9565–9568.

(22) Dong, B.; Cao, B. S.; He, Y. Y.; Liu, Z.; Li, Z. P.; Feng, Z. Q. Temperature Sensing and *In Vivo* Imaging by Molybdenum Sensitized Visible Upconversion Luminescence of Rare-Earth Oxides. *Adv. Mater.* **2012**, *24*, 1987–1993.

(23) Yang, Y. M.; Kong, W. Q.; Li, H.; Liu, J.; Yang, M. M.; Huang, H.; Liu, Y.; Wang, Z. Y.; Wang, Z. Q.; Sham, T.-K.; Zhong, J.; Wang, C.; Liu, Z.; Lee, S.-T.; Kang, Z. H. Fluorescent *N*-Doped Carbon Dots as *In Vitro* and *In Vivo* Nanothermometer. *ACS Appl. Mater. Interfaces* **2015**, *7*, 27324–27330.

- (24) Haro-González, P.; Ramsay, W. T.; Maestro, L. M.; del Rosal, B.; Santacruz-Gomez, K.; del Carmen Iglesias-de la Cruz, M.; Sanz-Rodríguez, F.; Chooi, J. Y.; Sevilla, P. R.; Bettinelli, M.; Choudhury, D; Kar K. A.; García-Solé, J.; Jaque D.; Paterson L. Quantum Dot-Based Thermal Spectroscopy and Imaging of Optically Trapped Microspheres and Single Cells. *Small* **2013**, *9*, 2162–2170.
- (25) Cui, Y. J.; Song, R. J.; Yu, J. C.; Liu, M.; Wang, Z. Q.; Wu, C. D.; Yang, Y.; Wang, Z. Y.; Chen, B. L.; Qian, G. D. Dual-Emitting MOF-Dye Composite for Ratiometric Temperature Sensing. *Adv. Mater.* **2015**, *27*, 1420–1425.
- (26) Shang, L.; Stockmar, F.; Azadfar, N.; Nienhaus, G. U. Intracellular Thermometry by Using Fluorescent Gold Nanoclusters. *Angew. Chem. Int. Ed.* **2013**, *52*, 11154–11157.
- (27) Cui, Y. J.; Zhu, F. L.; Chen, B. L.; Qian, G. D. Metal–Organic Frameworks for Luminescence Thermometry. *Chem. Commun.* **2015**, *51*, 7420–7431.
- (28) McLaurin, E. J.; Bradshaw, L. R.; Gamelin, D. R. Dual-Emitting Nanoscale Temperature Sensors. *Chem. Mater.* **2013**, *25*, 1283–1292.

- (29) McLaurin, E. J.; Vlaskin, V. A.; Gamelin, D. R. Water-Soluble Dual-Emitting Nanocrystals for Ratiometric Optical Thermometry. *J. Am. Chem. Soc.* **2011**, *133*, 14978–14980.
- (30) Saccomandi, P.; Schena, E.; Silvestri, S. Techniques for Temperature Monitoring during Laser-Induced Thermotherapy: An Overview. *Int. J. Hyperther.* **2013**, *29*, 609–619.
- (31) Cerón, E. N.; Ortgies, D. H.; del Rosal, B.; Ren, F.; Benayas, A.; Vetrone, F.; Ma, D. L.; Sanz-Rodríguez, F.; García-Solé, J.; Jaque, D.; Rodríguez, E. M. Hybrid Nanostructures for High-Sensitivity Luminescence Nanothermometry in the Second Biological Window. *Adv. Mater.* **2015**, *27*, 4781–4787.
- (32) Rocha, U.; Jacinto da Silva, C.; Ferreira Silva, W.; Guedes, I.; Benayas, A.; Martínez Maestro, L.; Acosta Elias, M.; Bovero, E.; van Veggel, F. C. J. M.; García-Solé, J. A.; Jaque, D. Subtissue Thermal Sensing Based on Neodymium-Doped LaF₃ Nanoparticles. *ACS Nano* **2013**, *7*, 1188–1199.

- (33) Marciniak, L.; Prorok, K.; Francés-Soriano, L.; Pérez-Prieto, J.; Bednarkiewicz, A. A Broadening Temperature Sensitivity Range with a Core–Shell YbEr@YbNd Double Ratiometric Optical Nanothermometer. *Nanoscale* **2016**, *8*, 5037–5042.
- (34) Yang, F.; Skripka, A.; Benayas, A.; Dong, X. K.; Hong, S. H.; Ren, F. Q.; Oh, J. K.; Liu, X. Y.; Vetrone, F.; Ma, D. L. An Integrated Multifunctional Nanoplatfrom for Deep-Tissue Dual-Mode Imaging. *Adv. Funct. Mater.* **2018**, *28*, 1706235.
- (35) Weissleder, R. A Clearer Vision for *In Vivo* Imaging. *Nat. Biotechnol.* **2001**, *19*, 316–317.
- (36) Bashkatov, A. N.; Genina, E. A.; Kochubey, V. I.; Tuchin, V. V. Optical Properties of Human Skin, Subcutaneous and Mucous Tissues in the Wavelength Range from 400 to 2000 nm. *J. Phys. D: Appl. Phys.* **2005**, *38*, 2543–2555.
- (37) Wang, F. F.; Wan, H.; Ma, Z. R.; Zhong, Y. T.; Sun, Q. C.; Tian, Y.; Qu, L. Q.; Du, H. T.; Zhang, M. X.; Li, L. L.; Ma, H. L.; Luo, J.; Liang, Y. Y.; Li, W. J.; Hong, G. S.; Liu,

L. Q.; Dai, H. J. Light-Sheet Microscopy in the Near-Infrared II Window. *Nat. Methods* **2019**, *16*, 545–552.

(38) Wan, H.; Yue, J. Y.; Zhu, S. J.; Uno, T.; Zhang, X. D.; Yang, Q. L.; Yu, K.; Hong, G. S.; Wang, J. Y.; Li, L. L.; Ma, Z. R.; Gao, H. P.; Zhong, Y. T.; Su, J.; Antaris, A. L.; Xia, Y.; Luo, J.; Liang, Y. Y.; Dai, H. J. A Bright Organic NIR-II Nanofluorophore for Three-Dimensional Imaging into Biological Tissues. *Nat. Commun.* **2018**, *9*, 1171.

(39) Hong, G. S.; Antaris, A. L.; Dai, H. J. Near-Infrared Fluorophores for Biomedical Imaging. *Nat. Biomed. Eng.* **2017**, *1*, 0010.

(40) Zhu, S. J.; Herraiz, S.; Yue, J. Y.; Zhang, M. X.; Wan, H.; Yang, Q. L.; Ma, Z. R.; Wang, Y.; He, J. H.; Antaris, A. L.; Zhong, Y. T.; Diao, S.; Feng, Y.; Zhou, Y.; Yu, K.; Hong, G. S.; Liang, Y. Y.; Hsueh, A. J.; Dai, H. J. 3D NIR-II Molecular Imaging Distinguishes Targeted Organs with High-Performance NIR-II Bioconjugates. *Adv. Mater.* **2018**, *30*, 1705799.

(41) Carvajal Marti, J. J.; Savchuk, O.; Nexha, A.; Pujol, M. C.; Aguiló, M.; Díaz, F. Berghmans, F., Mignani, A. G. Expanding Luminescence Thermometry Detection Range to the SWIR for Biomedical Applications. In *Optical Sensing and Detection V*, Eds.; SPIE: Strasbourg, France, 2018; p 34.

(42) Kamimura, M.; Matsumoto, T.; Suyari, S.; Umezawa, M.; Soga, K. Ratiometric Near-Infrared Fluorescence Nanothermometry in the OTN-NIR (NIR II/III) Biological Window Based on Rare-Earth Doped β -NaYF₄ Nanoparticles. *J. Mater. Chem. B* **2017**, *5*, 1917–1925.

(43) Sekiyama, S.; Umezawa, M.; Kuraoka, S.; Ube, T.; Kamimura, M.; Soga, K. Temperature Sensing of Deep Abdominal Region in Mice by Using Over-1000 nm Near-Infrared Luminescence of Rare-Earth-Doped NaYF₄ Nanothermometer. *Sci. Rep.* **2018**, *8*, 16979.

(44) Ximendes, E. C.; Santos, W. Q.; Rocha, U.; Kagola, U. K.; Sanz-Rodríguez, F.; Fernández, N.; Gouveia-Neto, A. da S.; Bravo, D.; Domingo, A. M.; del Rosal, B.; Brites,

C. D. S.; Carlos, L. D.; Jaque D.; Jacinto C. Unveiling *In Vivo* Subcutaneous Thermal Dynamics by Infrared Luminescent Nanothermometers. *Nano Lett.* **2016**, *16*, 1695–1703.

(45) Ximendes, E. C.; Rocha, U.; Sales, T. O.; Fernández, N.; Sanz-Rodríguez, F.; Martín, I. R.; Jacinto, C.; Jaque, D. *In Vivo* Subcutaneous Thermal Video Recording by Supersensitive Infrared Nanothermometers. *Adv. Funct. Mater.* **2017**, *27*, 1702249.

(46) Santos, H. D. A.; Ximendes, E. C.; Iglesias-de la Cruz, M. del C.; Chaves-Coira, I.; del Rosal, B.; Jacinto, C.; Monge, L.; Rubia-Rodríguez, I.; Ortega, D.; Mateos, S.; García-Solé, J. G.; Jaque, D.; Fernández, N. *In Vivo* Early Tumor Detection and Diagnosis by Infrared Luminescence Transient Nanothermometry. *Adv. Funct. Mater.* **2018**, *28*, 1803924.

(47) Ximendes, E. C.; Rocha, U.; del Rosal, B.; Vaquero, A.; Sanz-Rodríguez, F.; Monge, L.; Ren, F.; Vetrone, F.; Ma, D.; García-Solé, J.; Jacinto, C.; Jaque, D.; Fernández, N. *In Vivo* Ischemia Detection by Luminescent Nanothermometers. *Adv. Healthcare Mater.* **2017**, *6*, 1601195.

(48) del Rosal, B.; Ximendes, E.; Rocha, U.; Jaque, D. *In Vivo* Luminescence Nanothermometry: From Materials to Applications. *Adv. Opt. Mater.* **2017**, *5*, 1600508.

(49) Labrador-Páez, L.; Pedroni, M.; Speghini, A.; García-Solé, J.; Haro González, P.; Jaque, D. Reliability of Rare-Earth-Doped Infrared Luminescent Nanothermometers. *Nanoscale* **2018**, *10*, 22319–22328.

(50) Crawford, A. C.; Skuratovsky, A.; Porter, M. D. Sampling Error: Impact on the Quantitative Analysis of Nanoparticle-Based Surface-Enhanced Raman Scattering Immunoassays. *Anal. Chem.* **2016**, *88*, 6515–6522.

(51) Boyd, R. D.; Pichaimuthu, S. K.; Cuenat, A. New Approach to Inter-Technique Comparisons for Nanoparticle Size Measurements; Using Atomic Force Microscopy, Nanoparticle Tracking Analysis and Dynamic Light Scattering. *Colloids Surf., A* **2011**, *387*, 35–42.

(52) Garcia, M. A.; Fernandez Pinel, E.; de la Venta, J.; Quesada, A.; Bouzas, V.; Fernández, J. F.; Romero, J. J.; Martín González, M. S.; Costa-Krämer, J. L. Sources of

Experimental Errors in the Observation of Nanoscale Magnetism. *J. Appl. Phys.* **2009**, *105*, 013925.

(53) Grandke, J.; Resch-Genger, U.; Bremser, W.; Garbe, L.-A.; Schneider, R. J. Quality Assurance in Immunoassay Performance-Temperature Effects. *Anal. Methods* **2012**, *4*, 901-905.

(54) Wang, S.-Y.; Huang, S.; Borca-Tasciuc, D.-A. Potential Sources of Errors in Measuring and Evaluating the Specific Loss Power of Magnetic Nanoparticles in an Alternating Magnetic Field. *IEEE Trans. Magn.* **2013**, *49*, 255–262.

(55) Gaufrès, E.; Marcet, S.; Aymong, V.; Tang, N. Y.-W.; Favron, A.; Thouin, F.; Allard, C.; Rioux, D.; Cottenye, N.; Verhaegen, M.; Martel, R. Hyperspectral Raman Imaging Using Bragg Tunable Filters of Graphene and Other Low-Dimensional Materials: Hyperspectral Raman Imaging Using Bragg Tunable Filters of Graphene and Other Low-Dimensional Materials. *J. Raman Spectrosc.* **2018**, *49*, 174–182.

- (56) Mishra, P.; Asaari, M. S. M.; Herrero-Langreo, A.; Lohumi, S.; Diezma, B.; Scheunders, P. Close Range Hyperspectral Imaging of Plants: A Review. *Biosyst. Eng.* **2017**, *164*, 49–67.
- (57) Amigo, J. M.; Babamoradi, H.; Elcoroaristizabal, S. Hyperspectral Image Analysis. A Tutorial. *Anal. Chim. Acta.* **2015**, *896*, 34–51.
- (58) Bock, C. H.; Parker, P. E.; Cook, A. Z.; Gottwald, T. R. Visual Rating and the Use of Image Analysis for Assessing Different Symptoms of Citrus Canker on Grapefruit Leaves. *Plant Dis.* **2008**, *92*, 530–541.
- (59) Galassi, T. V.; Jena, P. V.; Shah, J.; Ao, G.; Molitor, E.; Bram, Y.; Frankel, A.; Park, J.; Jessurun, J.; Ory, D. S.; Haimovitz-Friedman, A.; Roxbury, D.; Mittal, J.; Zheng, M.; Schwartz, R. E.; Heller, D. A. An Optical Nanoreporter of Endolysosomal Lipid Accumulation Reveals Enduring Effects of Diet on Hepatic Macrophages *In Vivo*. *Sci. Transl. Med.* **2018**, *10*, 2680.

- (60) Star, W. M.; Marijnissen, J. P. A.; Gemert, M. J. C. van. Light Dosimetry in Optical Phantoms and in Tissues: I. Multiple Flux and Transport Theory. *Phys. Med. Biol.* **1988**, *33*, 437–454.
- (61) Sordillo, L. A.; Pu, Y.; Pratavieira, S.; Budansky, Y.; Alfano, R. R. Deep Optical Imaging of Tissue Using the Second and Third Near-Infrared Spectral Windows. *J. Biomed. Opt.* **2014**, *19*, 056004.
- (62) Gendrin, C.; Roggo, Y.; Collet, C. Pharmaceutical Applications of Vibrational Chemical Imaging and Chemometrics: A Review. *J. Pharm. Biomed. Anal.* **2008**, *48*, 533–553.
- (63) Gowen, A. A.; Feng, Y. Z.; Gaston, E.; Valdramidis, V. Recent Applications of Hyperspectral Imaging in Microbiology. *Talanta* **2015**, *137*, 43–54.
- (64) Mishra, P.; Herrero-Langreo, A.; Barreiro, P.; Roger, J. M.; Diezma, B.; Gorretta, N.; Lleó, L. Detection and Quantification of Peanut Traces in Wheat Flour by Near Infrared

Hyperspectral Imaging Spectroscopy Using Principal-Component Analysis. *J. Near Infrared. Spec.* **2015**, *23*, 15–22.

(65) Mishra, P.; Cordella, C. B. Y.; Rutledge, D. N.; Barreiro, P.; Roger, J. M.; Diezma, B. Application of Independent Components Analysis with the JADE Algorithm and NIR Hyperspectral Imaging for Revealing Food Adulteration. *J. Food Eng.* **2016**, *168*, 7–15.

(66) Matsuda, O.; Tanaka, A.; Fujita, T.; Iba, K. Hyperspectral Imaging Techniques for Rapid Identification of Arabidopsis Mutants with Altered Leaf Pigment Status. *Plant Cell Physiol.* **2012**, *53*, 1154–1170.

(67) Yakovliev, A.; Ziniuk, R.; Wang, D.; Xue, B.; Vretik, L. O.; Nikolaeva, O. A.; Tan, M.; Chen, G.; Slominskii, Yu. L.; Qu, J.; Ohulchanskyy T. Y. Hyperspectral Multiplexed Biological Imaging of Nanoprobes Emitting in the Short-Wave Infrared Region. *Nanoscale Res. Lett.* **2019**, *14*, 243.

- (68) Gowen, A.; Odonnell, C.; Cullen, P.; Downey, G.; Frias, J. Hyperspectral Imaging – An Emerging Process Analytical Tool for Food Quality and Safety Control. *Trends Food Sci. Technol.* **2007**, *18*, 590–598.
- (69) Bhatt, M.; Ayyalasomayajula, K. R.; Yalavarthy, P. K. Generalized Beer–Lambert Model for Near-Infrared Light Propagation in Thick Biological Tissues. *J. Biomed. Opt.* **2016**, *21*, 076012.
- (70) Sassaroli, A.; Fantini, S. Comment on the Modified Beer–Lambert Law for Scattering Media. *Phys. Med. Biol.* **2004**, *49*, N255–N257.
- (71) Kocsis, L.; Herman, P.; Eke, A. The Modified Beer–Lambert Law Revisited. *Phys. Med. Biol.* **2006**, *51*, N91–N98.
- (72) Son, I.-Y.; Yazici, B. Near Infrared Imaging and Spectroscopy for Brain Activity Monitoring. In *Advances in Sensing with Security Applications*; Byrnes, J., Ostheimer, G., Eds.; Kluwer Academic Publishers: Dordrecht, **2006**, *2*, 341–372.

(73) Marciniak, Ł.; Bednarkiewicz, A.; Stefanski, M.; Tomala, R.; Hreniak, D.; Strek, W.

Near Infrared Absorbing Near Infrared Emitting Highly-Sensitive Luminescent Nanothermometer Based on Nd³⁺ to Yb³⁺ Energy Transfer. *Phys. Chem. Chem. Phys.* **2015**, *17*, 24315–24321.

(74) Ogle, M. M.; Smith McWilliams, A. D.; Ware, M. J.; Curley, S. A.; Corr, S. J.; Martí,

A. A. Sensing Temperature *In Vitro* and in Cells Using a BODIPY Molecular Probe. *J. Phys. Chem. B* **2019**, *123*, 7282–7289.

(75) Doughty, A.; Hoover, A.; Layton, E.; Murray, C.; Howard, E.; Chen, W.

Nanomaterial Applications in Photothermal Therapy for Cancer. *Materials* **2019**, *12*, 779.

(76) van der Meer, F. J.; Faber, D. J.; Çilesiz, I.; van Gemert, M. J. C.; van Leeuwen,

T. G. Temperature-Dependent Optical Properties of Individual Vascular Wall Components Measured by Optical Coherence Tomography. *J. Biomed. Opt.* **2006**, *11*, 041120.

(77) Su, Y.; Yao, X. S.; Li, Z.; Meng, Z.; Liu, T.; Wang, L. Measurements of the Thermal Coefficient of Optical Attenuation at Different Depth Regions of *In Vivo* Human Skins Using Optical Coherence Tomography: A Pilot Study. *Biomed. Opt. Express* **2015**, *6*, 500–513.

(78) Laufer, J.; Simpson, R.; Kohl, M.; Essenpreis, M.; Cope, M. Effect of Temperature on the Optical Properties of *Ex Vivo* Human Dermis and Subdermis. *Phys. Med. Biol.* **1998**, *43*, 2479–2489.

(79) Vogt, W. C.; Barton, J. K.; Agrawal, A.; Pfefer, T. J. Measurement and Thermal Dependence of Biological Tissue Optical Properties. In *Theory and Applications of Heat Transfer in Humans*; Shrivastava, D., Ed.; John Wiley & Sons Ltd: Chichester, UK, **2018**; pp 355–378.

(80) Pettit, G. H.; Ediger, M. N.; Weiblinger, R. P. Dynamic Optical Properties of Collagen-Based Tissue during ArF Excimer Laser Ablation. *Appl. Opt.* **1993**, *32*, 488–493.

- (81) Çilesiz, I. F.; Welch, A. J. Light Dosimetry: Effects of Dehydration and Thermal Damage on the Optical Properties of the Human Aorta. *Appl. Opt.* **1993**, *32*, 477–487.
- (82) Pickering, J. W.; Bosman, S.; Posthumus, P.; Blokland, P.; Beek, J. F.; van Gemert, M. J. C. Changes in the Optical Properties (at 6328 nm) of Slowly Heated Myocardium. *Appl. Opt.* **1993**, *32*, 367–371.
- (83) Nilsson, A. M. K.; Lucassen, G. W.; Verkruysse, W.; Andersson-Engels, S.; van Gemert, M. J. C. Changes in Optical Properties of Human Whole Blood *In Vitro* Due to Slow Heating. *Photochem. Photobiol.* **1997**, *65*, 366–373.
- (84) Jerath, M. R.; Gardner, C. M.; Rylander, H. G.; Welch, A. J. Dynamic Optical Property Changes: Implications for Reflectance Feedback Control of Photocoagulation. *J. Photochem. Photobiol. B* **1992**, *16*, 113–126.

Table of Contents graphic

